A joint numerical study of multi-regime turbulent combustion

Document license:
CC BY

DOI:
10.1016/j.jaecs.2023.100221

Document status and date:
Published: 01/12/2023

Document Version:
Publisher's PDF, also known as Version of Record (includes final page, issue and volume numbers)

Please check the document version of this publication:

• A submitted manuscript is the version of the article upon submission and before peer-review. There can be important differences between the submitted version and the official published version of record. People interested in the research are advised to contact the author for the final version of the publication, or visit the DOI to the publisher's website.
• The final author version and the galley proof are versions of the publication after peer review.
• The final published version features the final layout of the paper including the volume, issue and page numbers.

Link to publication

Download date: 08. Feb. 2024

A joint numerical study of multi-regime turbulent combustion

Benoît Fiorina [a,*], Tan Phong Luu [a], Samuel Dillon [a,b], Renaud Mercier [b], Ping Wang [c], Lorenzo Angelilli [d], Pietro Paolo Ciottoli [e], Francisco E. Hernández–Pérez [d], Mauro Valorani [e], Hong G. Im [d], James C. Massey [f,g], Zhiyi Li [f], Zhi X. Chen [h], Nedunchezhian Swaminathan [f], Sebastian Popp [i], Sandra Hartl [i,j], Hendrik Nicolai [i], Christian Hasse [i], Andreas Dreizler [i], David Butz [i], Dirk Geyer [j], Adrian Breicher [j,i], Kai Zhang [k], Christophe Duwig [k], Weijie Zhang [l], Wang Han [m], Jeroen van Oijen [n], Arthur Péquin [o], Alessandro Parente [o], Linus Engelmann [p], Andreas Kempf [p], Maximilian Hansinger [q], Michael Pfitzner [q], Robert S. Barlow [r,i]

[a] Université Paris-Saclay, CNRS, CentraleSupélec, Laboratoire EM2C, 91190, Gif-sur-Yvette, France
[b] SAFRAN Tech, Digital Sciences & Technologies Department, Rue des Jeunes Bois, Châteaufort, 78114 Magny-Les-Hameaux, France
[c] Institute for Energy Research, Jiangsu University, China
[d] King Abdullah University of Science and Technology, Saudi Arabia
[e] Sapienza University of Rome, Italy
[f] Department of Engineering, University of Cambridge, Trumpington Street, Cambridge CB2 1PZ, United Kingdom
[g] Robinson College, University of Cambridge, Grange Road, Cambridge CB3 9AN, United Kingdom
[h] State Key Laboratory of Turbulence and Complex Systems, Aeronautics and Astronautics, College of Engineering, Peking University, Beijing 100871, China
[i] Technical University of Darmstadt, Germany
[j] Darmstadt University of Applied Sciences, Germany
[k] KTH, Royal Institute of Technology, Sweden
[l] Xi'an Jiaotong University, China
[m] Beihang University, China
[n] Eindhoven University of Technology, The Netherlands
[o] Université Libre de Bruxelles, Aero-Thermo-Mechanics Laboratory, École Polytechnique de Bruxelles, Avenue F.D Roosevelt 50, 1050, Brussels, Belgium
[p] University of Duisburg–Essen, Germany
[q] Universität der Bundeswehr München, Germany
[r] Barlow Combustion Research, CA, USA

ARTICLE INFO

ABSTRACT

This article presents a joint numerical study on the Multi Regime Burner configuration. The burner design consists of three concentric inlet streams, which can be operated independently with different equivalence ratios, allowing the operation of stratified flames characterized by different combustion regimes, including premixed, non-premixed, and multi-regime flame zones. Simulations were performed on three LES solvers based on different numerical methods. Combustion kinetics were simplified by using tabulated or reduced chemistry methods. Finally, different turbulent combustion modeling strategies were employed, covering geometrical, statistical, and reactor based approaches. Due to this significant scattering of simulation parameters, a conclusion on specific combustion model performance is impossible. However, with ten numerical groups involved in the numerical simulations, a rough statistical analysis is conducted: the average and the standard deviation of the numerical simulation are computed and compared against experiments. This joint numerical study is therefore a partial illustration of the community's ability to model turbulent combustion. This exercise gives the average performance of current simulations and identifies physical phenomena not well captured today by most modeling strategies. Detailed comparisons between experimental and numerical data along radial profiles taken at different axial positions showed that the temperature field is fairly well captured up to 60 mm from the burner exit. The comparison reveals, however, significant discrepancies regarding CO mass fraction prediction. Three causes may explain this phenomenon. The first reason is the higher sensitivity of carbon monoxide to the simplification of detailed chemistry, especially when multiple combustion regimes are encountered. The second is the bias introduced by artificial thickening, which overestimates the species' mass

production rate. This behavior has been illustrated by manufacturing mean thickened turbulent flame brush from a random displacement of 1-D laminar flame solutions. The last one is the influence of the subgrid-scale flame wrinkling on the filtered chemical flame structure, which may be challenging to model.

1. Introduction

Most novel combustion chambers promote stratified combustion regimes to limit the flame temperature while ensuring the flame stabilization [1]. In terms of turbulent combustion modeling, challenges are to handle multiple combustion regimes which differ from canonical models usually dedicated to either premixed or non-premixed flame structures [2].

A numerical combustion strategy results from modeling choices made at two levels, corresponding to chemistry simplification and turbulent combustion modeling. Indeed, because of the complexity of combustion chemistry, detailed chemical schemes must be first simplified before being implemented into a CFD solver. Three major routes, namely *reduced*, *tabulated* and *optimized* chemistry have been proposed to describe kinetic effects at a reduced computational cost [3]. *Reduced* chemistry aims to decrease the number of reactions and species involved in a detailed kinetic scheme by removing species and reactions that will not significantly affect targeted flame properties [4,5]. Further reduction of the kinetics can be achieved to find analytical relations between species by applying, for instance, a Quasi-Steady State Approximation (QSSA) [6,7]. *Tabulated chemistry* aims to express the thermochemical variables in a reduced chemical state space prior to a CFD computation [8]. Key issues of tabulated chemistry techniques are the generation of the chemical look-up table and the choice of coordinates. Because of their ease of implementation and low cost, flamelet-based tabulated chemistry methods are very popular for engineering applications [9]. However, the definition of the tabulated flamelet archetype, in general either premixed [10,11] or non-premixed [12,13], potentially limits the range of validity of the method to a single combustion regime [14]. Finally, *optimized* chemistry aims at generating small mechanisms (from 1 to 4 steps in general), whose kinetic rate parameters are optimized to capture global flame properties such as, for example, the burning velocity and flame temperature [15,16] but also pollutant formation [17].

Once the chemistry is simplified, there are also three main alternatives to model turbulent combustion, which are the *geometrical*, *statistical* or *reactor based* approaches [18]. *Geometrical* methods, which model the flame front by a surface wrinkled by the turbulence, are designed to capture the flame front propagation in premixed or stratified combustion regimes. Under resolution of the flame front, whose thickness is in general smaller than the grid size, is generally managed by artificial thickening [19] or filtering [20], while subgrid scale flame wrinkling is modeled [21,22]. *Statistical* approaches describes the impact of turbulence on thermochemical flame properties by introducing Filtered Density Functions, which can be either transported or presumed [23]. Finally *reactor based* approaches, which assume that combustion occurs at small dissipative scales, are adapted to distributed combustion regimes [24].

The multiple possible combinations of *simplified chemistry* and *turbulent combustion* sub-models as well as the intrinsic differences between the different CFD flow solvers will lead to disparate simulation results. The evaluation of simulation data quality is the main objective of the TNF Workshop [25] where research groups agree to compute well-defined, experimentally characterized, target flames by using different models and codes. Within this framework, five research groups performed Large Eddy Simulations of the TSF A turbulent stratified flame configuration [26]. Despite the use of different turbulent combustion models and solvers, most simulations agree on the mean flame brush position and on the temperature fields [27]. The impact on the pollutant prediction, was not addressed within that study.

This article presents the results of a new joint numerical study conducted on a novel target flame series stabilized on the Multi Regime Burner (MRB), designed at TU Darmstadt and Darmstadt UAS and measured both in Darmstadt and at Sandia National Laboratories [28]. The burner configuration allows the operation of stratified flames stabilized by the flow field with well defined inflow and boundary conditions, promoting different combustion regimes, including premixed, non-premixed and multi-regime flame zones. In addition to velocity, mixing, and temperature statistics, measurements now include data on the carbon monoxide mass fraction. Recently published simulations performed of the MRB highlighted the difficulty to predict CO because its formation involves various chemical time scales [28–30].

Ten numerical groups are here involved in the numerical simulations: Technische Universität Darmstadt, University of Cambridge, Université Paris Saclay, KAUST, KTH Royal Institute of Technology, Jiangsu University, Université Libre de Bruxelles, Universität Duisburg Essen, the group of Xi'an Jiaotong University, Beihang University and Eindhoven University of Technology, and Universität der Bundeswehr München. The objective is to partially illustrate the ability of e turbulent combustion modeling community on multi-regime flame simulations. As many numerical and modeling parameters differ among the simulations, this exercise does not allow a fine sub-model comparison. However, it aims to identify the physical phenomena which remain challenging to predict by most of the modeling strategies. Each group decided on its own numerical and modeling strategy, independently of the other simulations, as no specific guidance was given prior to the simulations. The analysis of the results will therefore not allow us to conclude on best practice. The explanations for the differences observed between the simulations should be considered as scenario suggestions rather than definitive conclusions.

The present work's originality relies on the possibility of showing the average and standard deviation of simulations thanks to the large amount of collected data. Definitive conclusions regarding turbulent combustion model parameters are impossible, as too many parameters change between numerical cases. However, this significant scattering of numerical and modeling strategies is also an advantage as it illustrates the strengths and weaknesses of the state-of-the-art. This exercise is especially interesting to the engineers in charge of the simulation of reactive systems.

The article is organized as follows. The MRB configuration is presented in Section 2, the different numerical and combustion modeling strategies are given in Section 3 and results are shown in Section 4. The analysis discusses first the ability of the simulations to qualitatively reproduce the flame lift-off. A comparison between simulations and experiments is then conducted for the velocity, the species and the temperature fields in both outer and inner flame regions, characterized by premixed dominant and multiple combustion regimes, respectively. A focus is made on the influence of artificial flame thickening on the CO prediction. Scatter plots of temperature and CO mass fraction are finally analyzed in the mixture fraction space.

2. The multi regime burner configuration

The MRB configuration, designed and experimentally studied by Butz et al. [28], is made of three concentric inlet streams, each characterized by its own equivalence ratio. A schematic view of the burner geometry is given in Fig. 1. A rich premixed flow of methane and air is injected through the center tube (called "jet"). This main injection stream is surrounded by two concentric annular tubes, called "slot 1" and "slot 2". Pure air is injected through "slot 1", while a lean premixed flow of methane/air characterized by an equivalence ratio of 0.8 is

Table 1

Composition of the numerical and experimental teams involved in the joint study. The colored text in the first row indicates the color of the corresponding curves in the radial profile comparisons.

Team	Institution 1	COLD	MRB18b	MRB26b
Exp	Technische Universität Darmstadt, *Germany* Darmstadt UAS, *Germany* Barlow Combustion Research, *USA*	✓	✓	✓
Num A	EM2C-CNRS, Université Paris-Saclay, *France* Safran Tech, *France*	✓		✓
Num B	Jiangsu University, *China*		✓	✓
Num C	KAUST, *Saudi Arabia* Sapienza University of Rome, *Italia*	✓	✓	✓
Num D	University of Cambridge, *United Kingdom* Peking University, *China*	✓	✓	✓
Num E	Technische Universität Darmstadt, *Germany*			✓
Num F	KTH, Royal Institute of Technology, *Sweden*	✓	✓	✓
Num G	Xi'an Jiaotong University , *China* Beihang University, *China* Eindhoven Univ. of Tech, *Netherlands*	✓	✓	✓
Num H	Université Libre de Bruxelles, *Belgium* BRITE, *Belgium*	✓		✓
Num I	University of Duisburg–Essen, *Germany*		✓	✓
Num J	Universiẗat der Bundeswehr M´unchen, *Germany*	✓	✓	
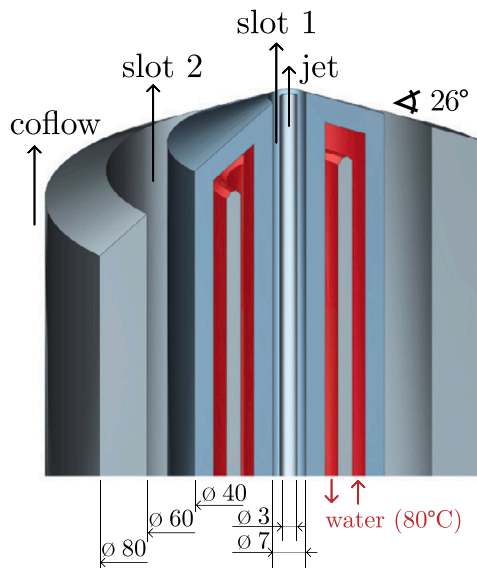
Fig. 1. MRB burner geometry.
Source: from [28].

injected through "slot 2". The temperature of the conical bluff body separating "slots 1" and "2" is regulated by water at 80 °C. Finally, a second bluff body separates "slot 2" from a low-speed air co-flow. Two operating conditions are computed here, namely MRB18b and MRB26b, which correspond to a main jet equivalence ratio of 1.8 and 2.6, respectively. For both cases, bulk velocities of the main jet, "slot 1" and "slot 2" streams are equal to 105 m/s, 15 m/s and 20 m/s, respectively. The high shear between the jet and "slot 1" induces fast mixing and the formation of the multi regime characteristics. A non-reactive flow configuration, called COLD, has also been measured under the same operating conditions as MRB18b [31].

Available experimental data include the velocity field measured from PIV [31] and the thermochemical flame structure given by Raman/Rayleigh/CO-LIF diagnostics [28]. From spatially resolved measurements of temperature, mixture fraction, and major species mass fraction, Butz et al. [28] analyzed the turbulent flame structure of the inner reaction zone by applying the Gradient Free Identification regime

criteria [37]. They mainly reported premixed flame archetypes near the burner exit for both MRB18b and MRB26b. Then, with increasing axial distance, the flame structure evolves with a growing importance of multi-regime structures, especially for MRB26b. Finally, while premixed flame regions remain dominant for the full length of MRB18b, non-premixed flame structures become significant in the downstream region of MRB26b, also observed numerically [30].

3. Numerical and combustion modeling strategies

3.1. Numerical set-up

The composition of the nine numerical and the experimental teams involved in the present study is indicated in Table 1 along with the cases computed by each group. The colored text in the first row indicates the color retained to distinguish the curves plotted later for radial profile comparisons. Table 2 details the corresponding numerical strategies. All groups conducted Large Eddy Simulations, including eight with the OpenFOAM solver and one each using the YALES2 [38] and PsiPhi [39] solvers. Simulations Num A and Num E employ the same grid, designed by TU Darmstadt [29]. Otherwise, a wide range of mesh resolution conditions is covered, with three orders of magnitude between the coarsest and finest grids composed of 1M and 2.2B elements, respectively. Four different models have been used to close the unresolved turbulent fluxes: WALE [34], K-equation, Sigma [32] and dynamic Smagorinsky [35]. For the given turbulent jet flow, non-reactive flow simulations presented in Supplementary Materials shows that the SGS closure of the filtered momentum equations does not significantly influence the prediction of the aerodynamic field.

3.2. Chemistry simplification

The combustion modeling strategies, given in Table 3, combine first a simplification of the detailed kinetics and then a modeling of subgrid scale interactions between the flame and the turbulence. As discussed in [3], simplified chemistry methods fall into three categories : (i) *reduced chemistry*, which aims to directly reduced the number of species and reactions from a detailed chemical mechanism, (ii) *tabulated chemistry*, where thermochemical quantities of interest are mapped in a low-order manifold and (iii) *optimized chemistry* which consist in designing an ad-hoc very small mechanism whose chemical rate constants have been optimized. As shown in Table 3, five groups

Table 2

Numerical strategies followed by the teams. The colored text in the first row indicates the color of the corresponding curves in the radial profile comparisons.

Team	LES solver	Grid (min spacing in mm)	Number of cells	Spatial scheme	Temporal scheme	Turbulent SGS
Num A	YALES2 Low Mach	Structured (0.1)	31 M (same as Num E)	4th order	4th order	Sigma [32]
Num B	OpenFOAM Compressible	Structured (0.02)	4.3 M	2nd order	2nd order	K-equation [33]
Num C	OpenFOAM Compressible	Structured (0.06)	64 M (MRB18b) 8 M (MRB26b)	2nd order	2nd order	WALE [34]
Num D	OpenFOAM Compressible	Structured (0.1)	3.5 M (same as Num H)	2nd order	1st order	Sigma [32]
Num E	OpenFOAM Low Mach	Structured (0.1)	31 M (same as Num A)	2nd order	2nd order	Sigma [32]
Num F	OpenFOAM Low Mach	Hybrid (0.27)	1 M	2nd order	2nd order	WALE [34]
Num G	OpenFOAM Low Mach	Structured (0.15)	3.8 M	2nd order	2nd order	Dyn. Smag. [35]
Num H	OpenFOAM Compressible	Structured (0.1)	3.5 M (same as Num D)	2nd order	2nd order	Smag. [36]
Num I	PsiPhi Low Mach	Structured (0.1)	2.2 B	4th order	3rd order	Sigma [32]
Num J	OpenFOAM Low Mach	Unstructured (0.05)	5.1M	2nd order	2nd order	WALE [34]

employs reduced schemes whereas the other five use a chemistry tabulation method. All chemical look-up tables are here generated from laminar flamelets: four from premixed 1-D laminar flames [11,40] and one from a non-premixed counterflow configuration [41,42]. The difference due to the nature of the chemistry simplification method will not be easily identified in the following result analysis as many other parameters are changing between simulations. This has however been already discussed in the literature, especially within a tabulated chemistry context [9,43].

3.3. Turbulent combustion modeling

As discussed previously, primary turbulent combustion modeling concepts are also classified in three categories, namely *reactor based*, *statistical* and *geometrical* approaches. As indicated in Table 3, the three simulations which model the SGS combustion using Partially Stirred Reactor (PaSR) [44,45] or Eddy Dissipation Concept (EDC) [46] models fall into the *reactor based* category. *Statistical* approaches are followed by two teams which employ a standard presumed Filtered Density Function (FDF) to close the filtered chemical reaction rate. Interestingly, all groups who prefer a *geometrical* description of the flame front manage the under-resolution with the popular Thickened Flame model for LES (TFLES) [19] also known as the Artificially Thickened flame model (ATF) [26]. A dynamic formulation of the thickening factor is retained with a flame sensor to limit artificial thickening to reacting layers. For all groups choosing such *geometrical* approach, the impact of the turbulence on the flame wrinkling at the SGS scale is captured with the Charlette model [21]. Only one group neglect subgrid scale turbulent effects on the chemistry.

3.4. Boundary conditions

The numerical teams followed different strategies to define the boundary conditions. The Technical University of Darmstadt performed a cold flow LES of the injector pipes. The solution of this precursor simulation has been used in *Num A*, *Num E* and *Num G* to prescribe the inlet flow velocity of main jet and slot 2, while a laminar parabolic profile has been set for slot 1. Other groups independently defined the boundary conditions, as described in Supplementary Material.

Fig. 2 compares all computed mean and RMS axial flow velocity profiles, taken 3 mm above the burner outlet. Black symbols with error bars indicate experimental measurements and uncertainties. Each thin colored solid line represents the solution obtained by one of the nine groups involved in the joint study as indicated in Table 1. Most of the simulations correctly recovered the velocity profiles at the burner exit, validating their respective inlet flow velocity parameters. Num B solution however overestimates the mean and RMS velocity profiles at the centerline. As indicated in the Supplementary Materials, the flow upstream the jet inflow is computed in group B simulation. The quality of the mesh in the tube may however not be sufficient to properly compute the turbulent pipe flow. This explains the bias observed in Fig. 6.

All groups prescribed a main jet composition corresponding to equivalence ratio $\phi = 2.6$ ($\phi = 1.8$) in configurations MRB26b (MRB18b), while pure air has been injected through slot 1. The set-up of slot 2 composition is however controversial because of a slight experimental inconsistency between the flow controllers signal and the Raman species measurements. Indeed, the mixture fraction measured at the exit of slot 2 with Raman technique ($Z_{expe} \approx 0.047$) does not exactly correspond to the equivalence ratio of 0.8 ($Z_{\phi=0.8} \approx 0.044$) *a priori* indicated by the flowmeters. This difference generated confusion among numerical teams who adopted different strategies: *Num B*, *Num C* and *Num E* imposed $Z_{slot2} = 0.047$ to fit the species measurements while the other teams set up $Z_{slot2} = 0.044$ as indicated by the flow controllers.

Two LES of the reactive MRB26 cases have been conducted to quantify the sensitivity to Z_{slot2}. Both simulations have been performed with YALES 2 solver on the TUD grid with a premixed flamelet model combined with TFLES (Num A). Only the value of Z_{slot2} is changed between the two simulations.

Computed mean radial profiles of the mixture fraction are compared against experimental data for both cases ($Z_{slot2} = 0.047$ and $Z_{slot2} = 0.044$) in the expanded view shown Fig. 3(a). Radial profiles of mixture fraction taken 6 mm above the burner exit show that, as expected, with $Z_{slot2} = 0.044$, the mixture fraction radial profiles underpredict the Raman measurements taken above slot 2 exit (20 mm < r < 30 mm). This is corrected by $Z_{slot2} = 0.047$ simulation. Interestingly, the mixture fraction in the recirculation zone (4 mm < r < 20 mm) becomes to be impacted by the change of slot 2 composition only from $h = 30$ mm. For $h = 6$ mm and $h = 15$ mm, the recirculating burnt gases mixture fraction remains slightly under estimated by the simulation.

Table 3

Chemistry simplification and turbulent combustion models employed by the teams. The colored text in the first row indicates the color of the corresponding curves in the radial profile comparisons. ARC: Analytically Reduced Chemistry; D-TFLES; Dynamical artificial Thickened Flame model for LES, EDC: Eddy Dissipation Concept, FWM: Flame Wrinkling Model, RC: Reduced Chemistry, TC: Tabulated Chemistry.

Team	Simp. Chem. model	Turb. Comb. model	Simp. Chem. category	Turb. Comb. category
Num A	Premixed flamelet tabulation [11,40]	D-TFLES [19,26] with FWM [21]	TC	Geometrical
Num B	15-species ARC [47]	D-TFLES [19] with FWM [21]	RC	Geometrical
Num C	15-species ARC [48]	EDC [46]	RC	Reactor based
Num D	Premixed flamelet tabulation [11,40] with transported Y_{CO} [30]	Presumed FDF [49–51]	TC	Statistical
Num E	Premixed flamelet tabulation [11,40] with transported Y_{CO} [29]	D-TFLES [19,26] with FWM [21]	TC	Geometrical
Num F	17 species skeletal mechanism [53]	PaSR [44,45,52]	RC	Reactor based
Num G	Non-premixed flamelet tabulation [41]	Presumed FDF [54,55]	TC	Statistical
Num H	15-species ARC mechanism [48]	PaSR [44,45,52]	RC	Reactor based
Num I	Premixed flamelet tabulation [11,40]	D-TFLES [19,26] with FWM [21]	TC	Geometrical
Num J	19 species ARC [56]	No model	RC	–

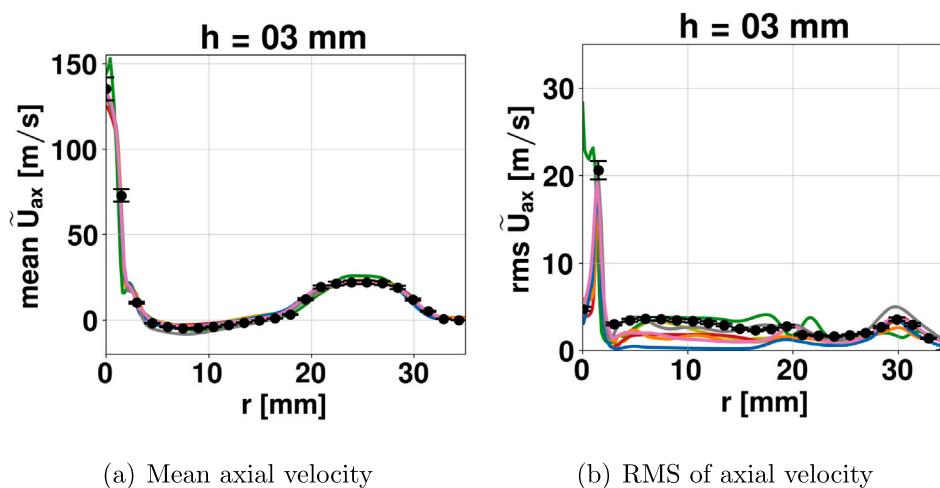(a) Mean axial velocity (b) RMS of axial velocity

Fig. 2. Mean and RMS radial profiles of the axial flow velocity in the MRB26b case, 3 mm above the burner exit. Black symbols: experiments. Black error bars: measurement uncertainty. Colored solid lines : Solutions from cases given in Table 1. (For interpretation of the references to colour in this figure legend, the reader is referred to the web version of this article.)

Fig. 3(b) shows a minor effect on the temperature profiles. Only the expanded view shown in Fig. 3(c) reveals a bias of approximately 50 K within the burnt gases recirculation zone from $h = 30$ mm. This is retrieved through adiabatic thermo-chemical equilibrium computations which indicate that the differences in element composition induced by ΔZ_{slot2} cause a similar bias of burnt gas temperature. Finally Fig. 3(d) show a minor impact of slot 2 composition on the CO mass fraction, where only the peak in the outer flame is affected. The impact of Z_{slot2} uncertainties remains then moderate.

Adiabatic conditions have been assumed at the wall boundaries by all groups. This assumption has been justified by complementary TUD simulations, which showed that accounting for heat losses at the burner lip separating the main jet from slot 1 does not significantly affect the turbulent structure of the flame [57].

Further information are give in the Supplementary Materials, where the numerical and modeling set-up are detailed group by group.

4. Results

4.1. Cold flow simulations

As indicated in Table 1, eight groups perform the cold flow simulation. Comparisons between experimental data and numerical results are presented in the supplementary materials. Despite the significant variation in the numerical scheme, grid quality, and turbulent SGS closures between simulations, a good agreement is reached between the simulations and the measurements. This observation suggests that the differences later observed in the reactive cases will mainly be due to the flame computing (including combustion modeling and numerical resolution of the reactive layer).
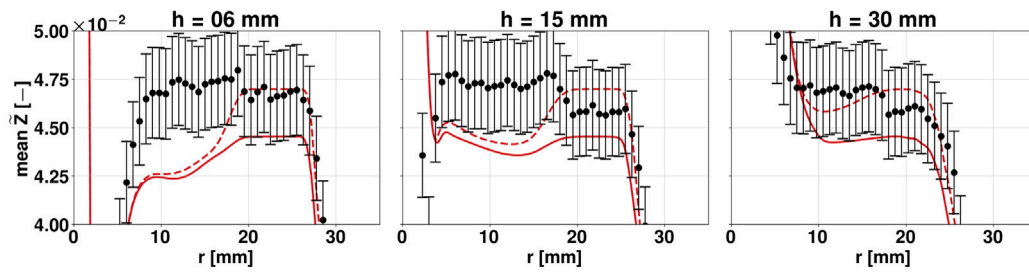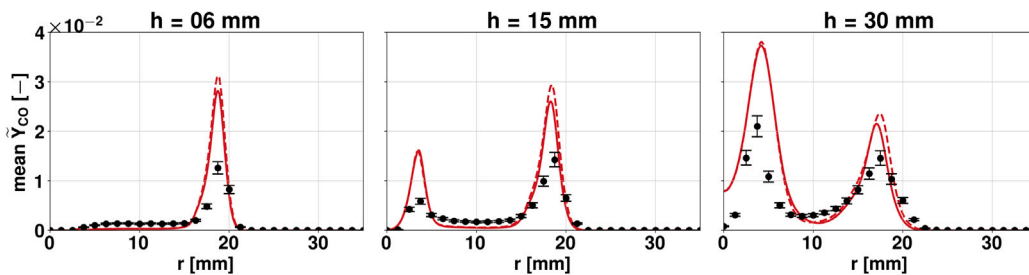
(a) Mean mixture fraction (expanded view)
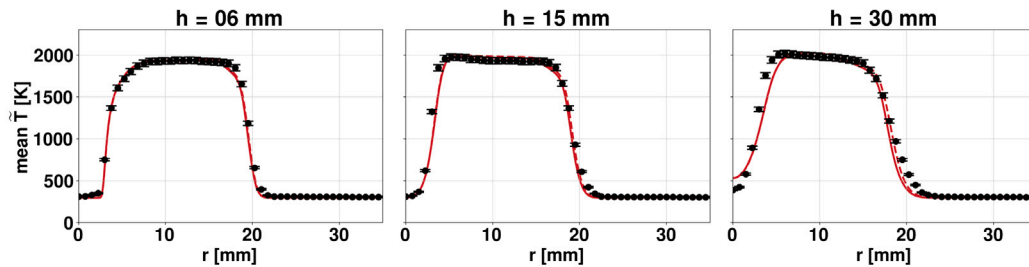
(b) Mean temperature
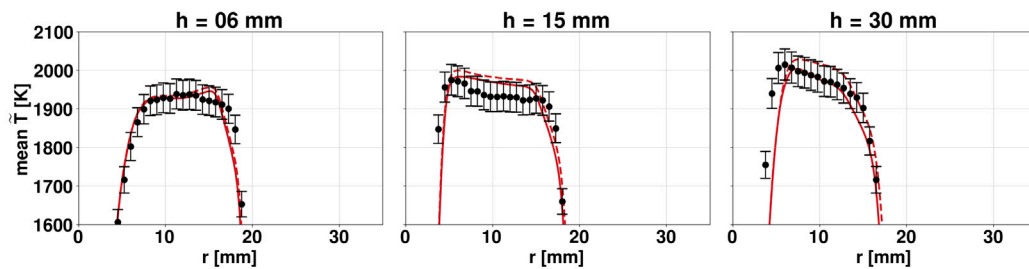
(c) Mean temperature (expanded view)

(d) Mean CO mass fraction

Fig. 3. Sensitivity analysis of the fresh gas composition injected through slot 2 on the mean radial profiles. Black symbols: experiments. Black error bars: measurement uncertainty. Solid lines : numerical solutions with $Z_{slot2} = 0.04454$. Dashed lines: numerical solutions with $Z_{slot2} = 0.047$. (For interpretation of the references to colour in this figure legend, the reader is referred to the web version of this article.)

4.2. Flame topology and lift-off

Instantaneous snapshots of 2-D temperature iso-contour are shown in Fig. 4 for a selection of 8 computations, ordered by grid size from left to right and top to bottom. The same grey scale has been adopted ranging from 300 K (black color) to 2300 K (white color). All simulations predict the recirculation zone, filled with hot burnt gases, which is formed behind the bluff-body. The influence of the mesh resolution on the turbulent flame structure is clearly evidenced; while the flame computed on the very coarse grid is almost not perturbed by

the flow, the highly resolved flames exhibit a very fine level of resolved flame wrinkling. Differences are evidenced on the jet penetration whose length seems sensitive to the grid resolution. Fig. 5 shows 2-D views of the progress variable reaction rate, where black and white color correspond to 0 and peak value, respectively. A quantitative comparison of the images is not possible, as each group used different progress variable definitions. It is however observed that all simulations retrieve the two main reaction zones identified in the experiments [28]:

- An outer reaction zone is stabilized by the burnt products recirculating behind the bluff-body and consumes reactant from slot
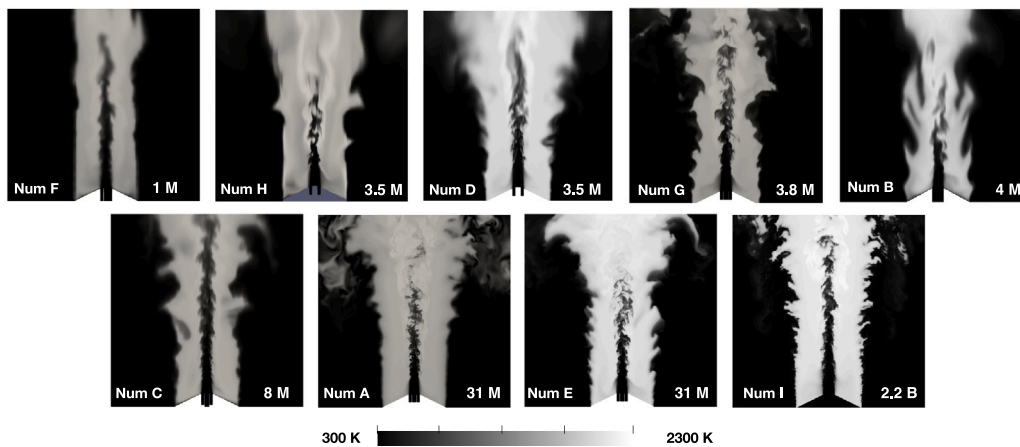
Fig. 4. 2D iso-contour of temperature extracted from nine simulations of MRB26b case. Increasing mesh size from left to right and top to bottom. Numerical team and number of grid elements are indicated on the bottom left and right corners of each figure, respectively.
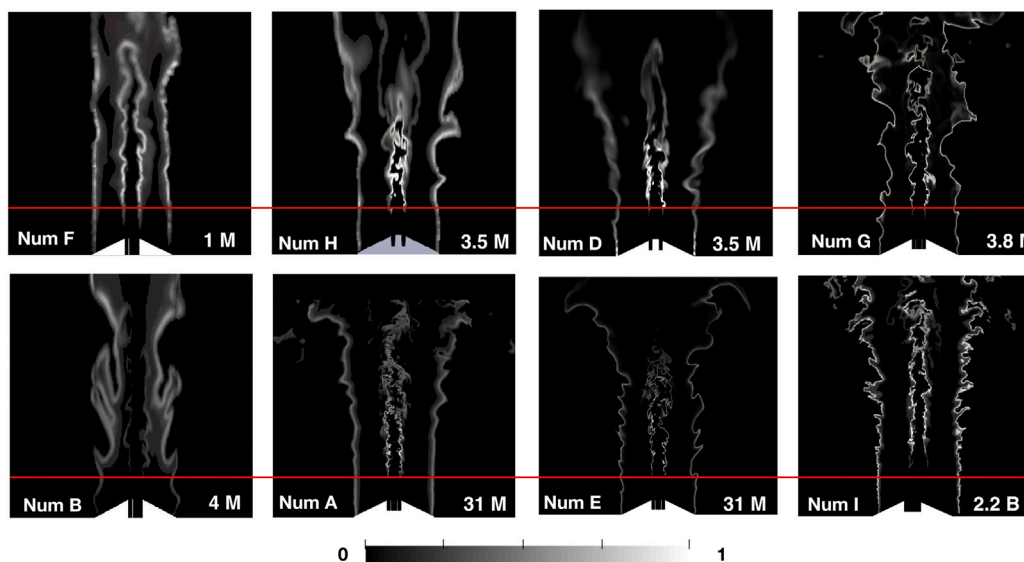

Fig. 5. 2D iso-contour of normalized progress variable reaction rate extracted from eight simulations of MRB26b case, with increasing mesh size from left to right and top to bottom. The reaction rate was normalized so that the maximum value corresponds to 1. Numerical team and number of grid elements are indicated on the bottom left and right corners of each figure, respectively. The solid red horizontal line is positioned arbitrarily at a given axial position to facilitate visual comparison of flame lift off heights. The source term has been divided by the thickening factor for TFLES simulations (Num A, Num E and Num I).

2. As the fresh equivalence ratio is within the flammability range of methane–air, the combustion regime is dominantly premixed here.

- An inner lifted flame downstream of the jet and slot 1 is supported by hot products and exposed to high stratifications. The GRFI analysis conducted [28] showed that this reaction zone exhibits a very complex turbulent flame dominated by multi-regime structures interacting with both premixed and non-premixed local flame zones.

The recent analysis performed from flow field and flame front tracking measurements [31] explained the stabilization mechanism. A mixture within flammability limits is first generated in the shear layer located between slot 1 and the central fuel jet. In the meantime, the recirculation zone behind the bluff body, filled with burnt gases produced by the outer lean flame, entrains hot products toward this flammable mixture. The combined increase of flame speed due to the high turbulence levels and elevated temperature in the shear layer then allow a lifted flame to stabilize above the jet and slot 1. Instantaneous 2D views of the progress variable reaction rate show that all simulations predicted well a lifted flame structure. Most of the numerical solutions

quite well agree on the position of the inner flame front tip (indicated by the horizontal red solid line). Only *Num F* predicts a very low lift-off height, which can be attributed to a poor grid resolution.

4.3. Radial profiles

Similar observations have been made when analyzing numerical data from MRB18b and MRB26b, therefore only computational results from MRB26b are discussed in the following sections. Mean radial profiles from MRB18b are available in Supplementary Materials.

Mean and RMS of the axial and radial components of the velocity field are shown in Fig. 6 for the case MRB26b. Results are plotted over the radius direction at four axial positions: h = 6, 15, 30 and 60 mm. The colors corresponding to each simulation are indicated in Table 1 and reminded in the color key embedded in the top of the figure. As many parameters are changing between the simulations (grid, numerical methods, BC's, subgrid closures models, etc.), a curve-by-curve analysis is of little interest, that is why the color key will not be repeated in the following figures. However, since we are fortunate to have ten numerical solutions, a rough statistical analysis is possible.
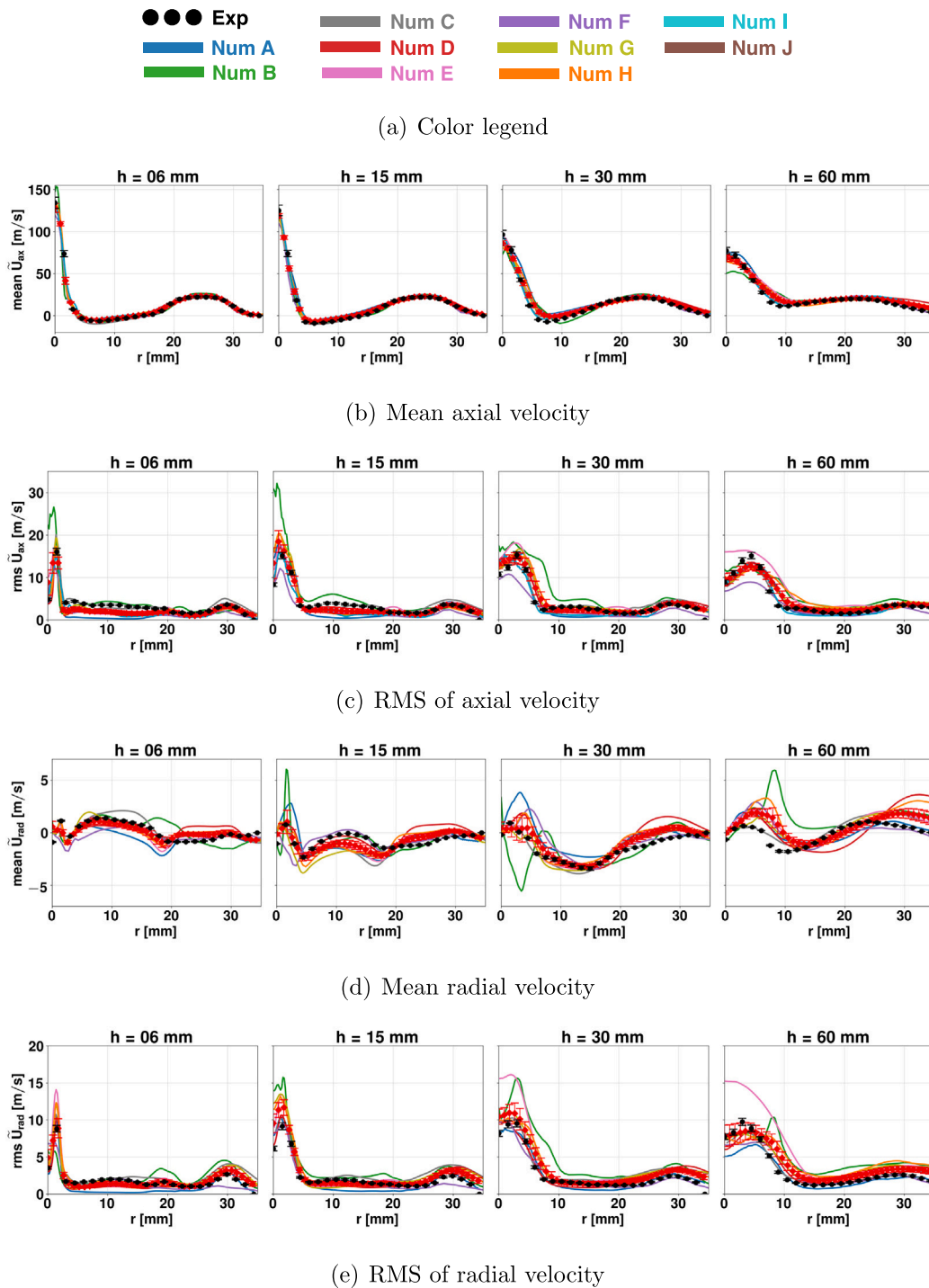
(a) Color legend

(b) Mean axial velocity

(c) RMS of axial velocity

(d) Mean radial velocity

(e) RMS of radial velocity

Fig. 6. Flow velocity in the MRB26b case. Black symbols: experiments. Black error bars: measurement uncertainty. Colored solid lines : Solutions from cases given in Table 1. Red symbols: average of all numerical solutions. Red vertical error bars: amplitude of the standard deviation of the simulations. (For interpretation of the references to colour in this figure legend, the reader is referred to the web version of this article.)

The red symbols are then the average of the nine individual solutions while the red vertical error bars indicate the amplitude of the standard deviation of the simulations. Mean and RMS of axial velocity are remarkably well predicted by all groups while radial velocity fields remains satisfactorily captured, although an overestimation is observed downstream, in the outer flame region. Significant discrepancies are however observed between Num B and other group solutions. This bias is attributed to the misprediction of the inflow boundary condition discussed previously. The error propagates downstream and affect the

quality of the shear layer prediction. As expected, simulations performed on the finest grid (Num I) leads to an excellent prediction of the flow field.

Despite such discrepancies, these results illustrate the general ability of LES flow solvers to capture the flow dynamical of jet flames, as observed in the previous TNF joint study [27].
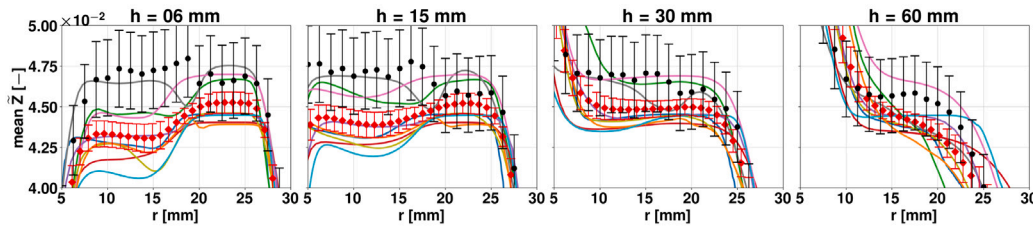
Mean and RMS radial profiles of the mixture fraction, plotted in Fig. 7, are well predicted by the simulations. In particular, simulations conducted on the finest mesh (Num I) present the best agreement. However, the expanded view (Fig. 7c) shown behind the bluff-body,
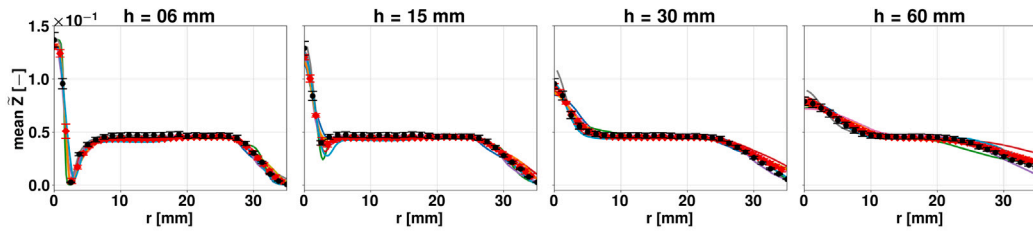
(a) Mean mixture fraction
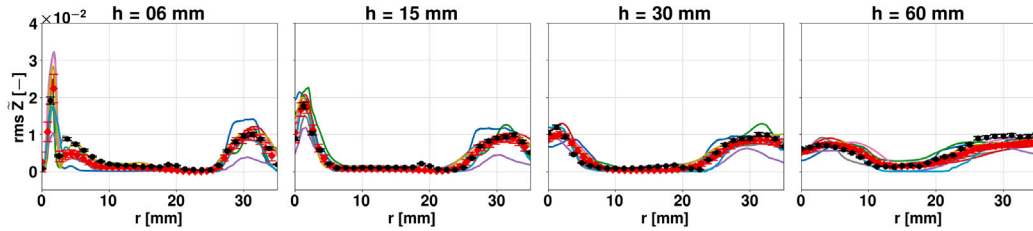
(b) RMS of mixture fraction

(c) Mean mixture fraction (zoom in the recirculation zone)

Fig. 7. Mixture fraction in the MRB26b case. Black symbols: experiments. Black symbols: experiments. Black error bars: measurement uncertainty. Colored solid lines : Solutions from cases given in Table 1. Red symbols: average of all numerical solutions. Red vertical error bars: amplitude of the standard deviation of the simulations. (For interpretation of the references to colour in this figure legend, the reader is referred to the web version of this article.)

in the flow recirculating between slot 1 and slot 2, reveals significant disagreements in the element composition. The reason is the differences in the composition of the mixture injected through the slot 2, as discussed previously in Section 3.4.

Fig. 8 shows the mean and RMS radial profiles of temperature fields. The inner flame front position (3 mm < r < 8 mm) is well computed at the first three axial positions: $h = 6$, 15 and 30 mm. Indeed, the average of the computations matches the experimental measurements while the numerical variance remains comparable with the experimental uncertainty. The outer flame (17 mm < r < 22 mm) is also fairly captured even if the simulations present a larger dispersion.

Discrepancies are more pronounced downstream, at $h = 60$ mm. In addition to disagreeing on average with the experiments, simulations exhibit a very large scatter. Note that the misprediction of the outer flame front position is correlated to the computing errors of the radial velocity previously observed in Fig. 6. The finely resolved grid (Num I) performs less in terms of temperature than the flow and mixing fields. This is assumed to be a consequence of lack of heat transfer modeling in the burner cap and the use of less accurate chemistry and turbulent combustion models.

Fig. 6(c) shows that, in the outer flame region, resolved RMS of temperature are below the measured data. As the plotted LES RMS does not include the subgrid scale RMS, conclusions regarding the simulation performances in terms of flame turbulence interactions are difficult.

However, it is observed that LES RMS remains lower than measured RMS, as expected from theory.

The expanded view in the bluff-body region shown in Fig. 8 (bottom) presents a deviation of the computed temperature from the measurements in the recirculation zone which can reach 250 K. A first possible explanation is the under-prediction of the mixture fraction, highlighted in Fig. 7(c). This might be due to some additional air entrainment from slot 1 or by the unity Le assumption, which leads to the under-prediction of the species accumulation in the recirculation zone as pointed out in [58–60]. Other possible source of error are the chemistry reduction method or the turbulent combustion model closures assumptions. Finally heat losses at the burner lips may also have a small impact. Complementary discussions on the difficulty to simulate the temperature field in the MRB configuration are available in [61].

Mean and RMS radial profiles of CO mass fraction are shown in Fig. 9. CO is present in the outer flame front (17 mm < r < 22 mm) starting from the burner exit, but starts to be produced in the inner reactive layer (3 mm < r < 8 mm) farther downstream from $h = 15$ mm. While computed mean CO profiles are close to experimental data, the dispersion of the simulation data is very high: the numerical uncertainty of the computed peak of CO mass fraction is about 30%–40% for both inner and outer flame fronts. The reason of these differences are discussed first in the outer flame front and then in the inner flame front.
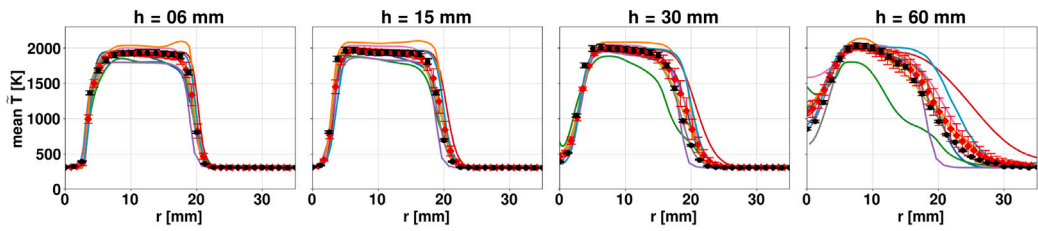
(a) Mean temperature
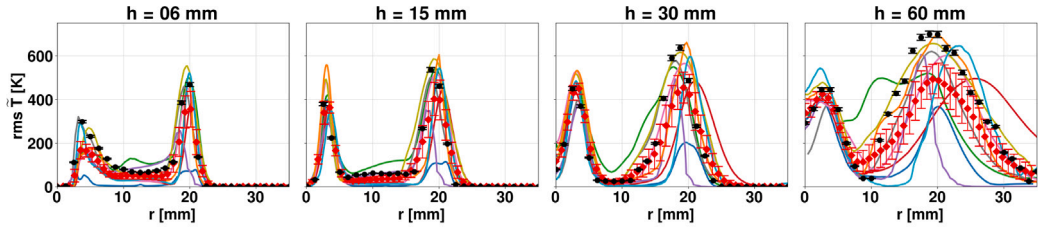
(b) RMS of temperature
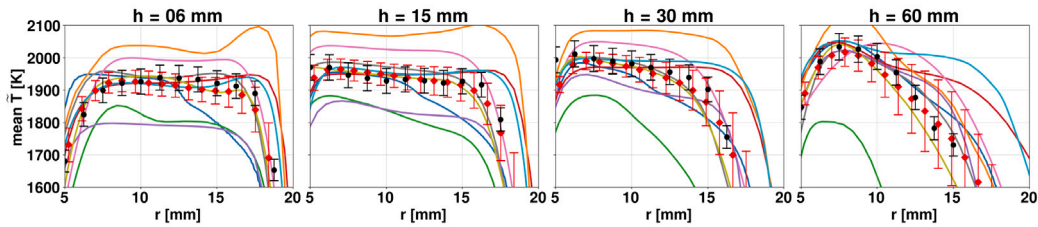
(c) Mean temperature (zoom in the recirculation zone)

Fig. 8. Temperature in the MRB26b case. Black symbols: experiments. Black error bars: measurement uncertainty. Colored solid lines : Solutions from cases given in Table 1. Red symbols: average of all numerical solutions. Red vertical error bars: amplitude of the standard deviation of the simulations. (For interpretation of the references to colour in this figure legend, the reader is referred to the web version of this article.)
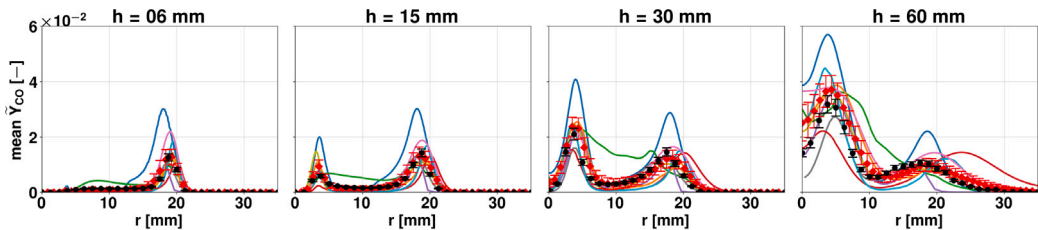
(a) Mean CO mass fraction
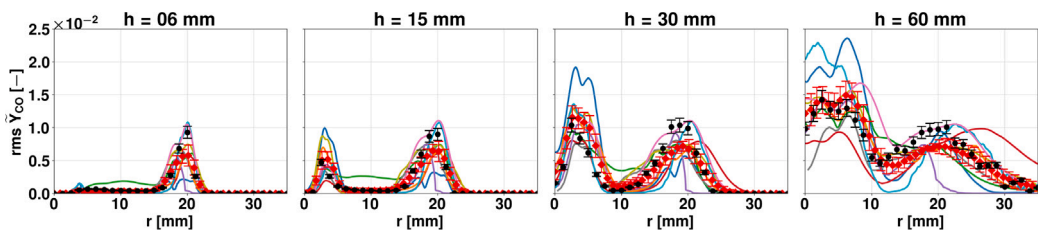
(b) RMS of CO

Fig. 9. CO mass fraction in the MRB26b case. Black symbols: experiments. Black error bars: measurement uncertainty. Colored solid lines : Solutions from cases given in Table 1. Red symbols: average of all numerical solutions. Red vertical error bars: amplitude of the standard deviation of the simulations. (For interpretation of the references to colour in this figure legend, the reader is referred to the web version of this article.)
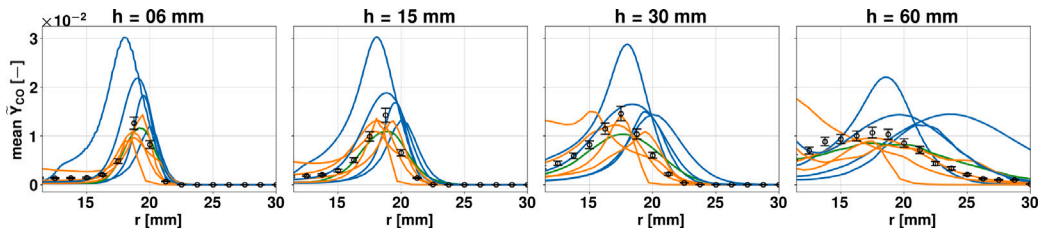
Fig. 10. Mean radial profiles of CO mass fraction in the MRB26b case sorted by the type of simplified chemistry model. Zoom in the outer flame region. Symbols: experimental data. Blue solid lines: premixed based tabulated chemistry. Green solid lines: non-premixed based tabulated chemistry. Orange solid lines: reduced chemistry. (For interpretation of the references to colour in this figure legend, the reader is referred to the web version of this article.)
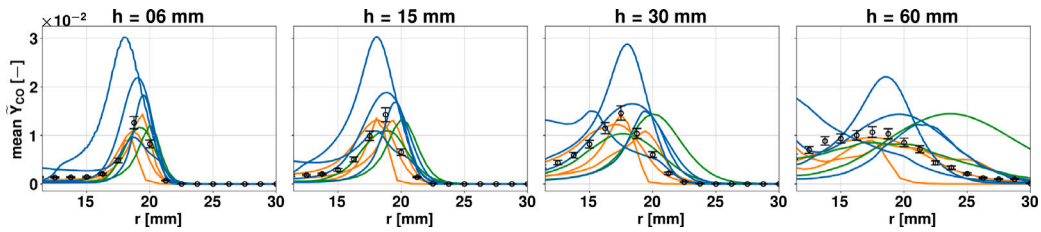

Fig. 11. Mean radial profiles of CO mass fraction in the MRB26b case sorted by the type of turbulent combustion model. Zoom in the outer flame region. Symbols: experimental data. Blue solid lines: geometrical. Green solid lines: statistical. Orange solid lines: reactor based. (For interpretation of the references to colour in this figure legend, the reader is referred to the web version of this article.)
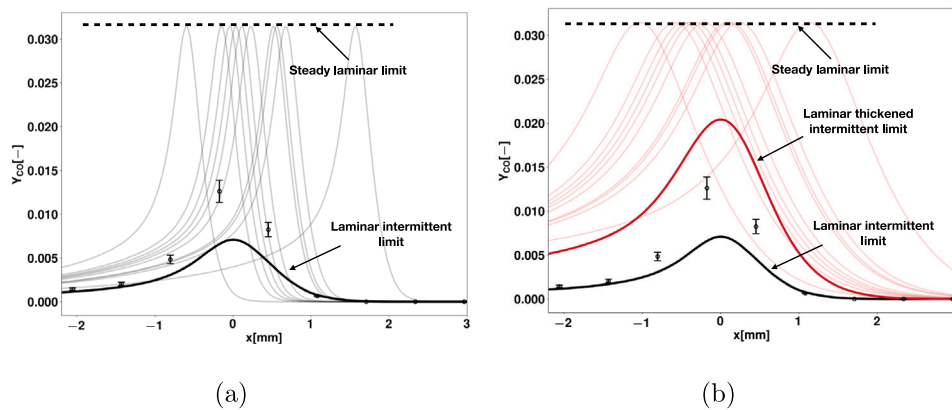

Fig. 12. Manufactured pseudo 1-D turbulent flame brush whose thickness matches the one measured 6 mm downstream the burner exit. Thin lines show a sample of the randomly distributed flamelet solutions. Bold lines are the Reynolds averaged mean profiles. Symbols are the experimental data measured at *h* = 6 mm. Left: without artificial flame thickening (F = 1). Right: with artificial flame thickening (F = 4).
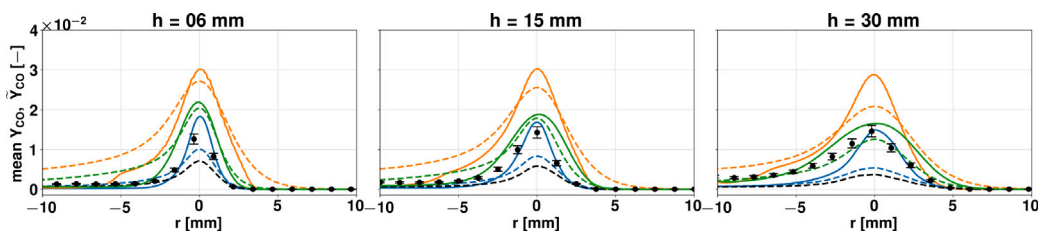

Fig. 13. Comparison between LES solutions computed with TFLES model and the corresponding mean manufactured thickened flame solutions. Solid lines: LES solutions. Dashed lines: manufactured solutions. Symbols: experimental data. Black: F = 1 (no-thickening). Blue: F = 1.5 (*Num I*). Green: F = 4 (*Num D*). Orange: F = 8.5 (*Num A*). (For interpretation of the references to colour in this figure legend, the reader is referred to the web version of this article.)

4.4. Outer flame analysis: on the impact of artificial flame thickening on the CO mass fraction

The analysis first focuses on the outer flame reactive layer, characterized by a standard turbulent premixed regime. Fig. 10 sorts the numerical solution by simplified chemistry methods. Most of the four reduced chemistry solutions (orange solid lines) give satisfactory estimates of the peak of CO, especially at the first three axial positions.

Surprisingly, the premixed-based tabulated chemistry approaches (blue solid lines) significantly over-predict the carbon monoxide production. This results is not consistent with previous analysis [14,43] which concluded that FPI or FGM should capture accurately the chemical structure of premixed flame reaction zone. To understand the reason of this deviation, results are now sorted by turbulent combustion models in Fig. 11. While statistical and reactor based results are distributed around the experimental data, the three solutions issued from the
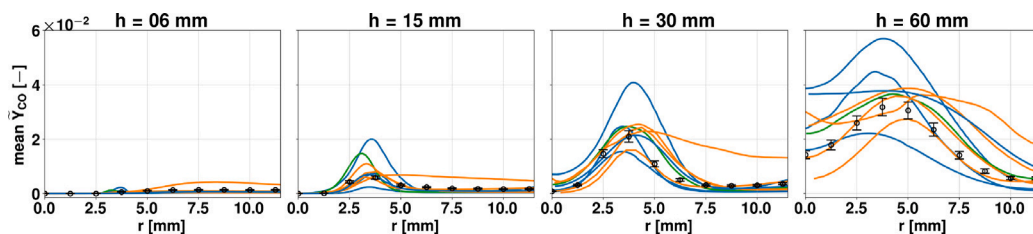
Fig. 14. Mean radial profiles of CO mass fraction in the MRB26b case sorted by the type of simplified chemistry model. Zoom in the inner flame region. Symbols: experimental data. Blue solid lines: premixed based tabulated chemistry. Green solid lines: non-premixed based tabulated chemistry. Orange solid lines: reduced chemistry. (For interpretation of the references to colour in this figure legend, the reader is referred to the web version of this article.)
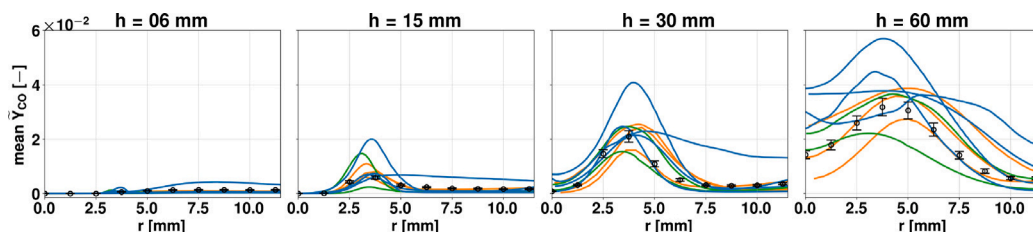

Fig. 15. Mean radial profiles of CO mass fraction in the MRB26b case sorted by the type of turbulent combustion model. Zoom in the inner flame region. Symbols: experimental data. Blue solid lines: geometrical. Green solid lines: statistical. Orange solid lines: reactor based. (For interpretation of the references to colour in this figure legend, the reader is referred to the web version of this article.)

geometrical approach (blue solid lines) significantly over predict the experimental measurement of CO mass fraction. For these three computations, the flame front under-resolution has been managed with an artificial thickening of the flame front. This mathematical operation retrieves the correct flame consumption speed but does not conserve the species mass as discussed in [62]. Recent LES of turbulent premixed flames observed that it may cause significant over-predictions of intermediates species peak values, such as the CO, in the flame brush [63,64].

An illustration of this effect is obtained by manufacturing a mean, pseudo 1-D, flame brush from a large number of laminar flamelets, following the idea suggested by Vervisch et al. [65]. A synthetic turbulent flame is manufactured by a random distribution of 5 000 detailed chemistry premixed laminar flamelet solutions. All solutions are identical (same thickness and chemical structure) but are localized at different positions. This procedure mimics a 1-D DNS performed in the flamelet regime as flamelet profiles are transported by turbulence without modification of their internal structure.

Fig. 12(a) shows an example of premixed flamelet distribution whose statistical properties have been adjusted to match the flame brush thickness, measured in the outer flame reaction zone at $h = 6$ mm and defined here as $\delta_{\widetilde{T}} = (\widetilde{T}_{Exp}^{BG} - \widetilde{T}_{Exp}^{FG})/(\max(d\widetilde{T}/dx)$, where superscripts FG and BG denotes fresh and burnt gases conditions, respectively. Averaging this ensemble of planar flame solutions provides a mean CO profile shown by the bold black solid line, which only accounts for the intermittency property of the flame brush.

Assuming flamelet regime, the 3-D wrinkling patterns tends to increase the averaged mass of CO. This phenomena, extensively discussed in [66], has been observed both by post-processing 3-D DNS of the Preccinsta burner solution [67] and by filtering filtered-wrinkled manufactured flamelets. The lower limit of CO production is therefore given by the average of planar (not wrinkled) 1-D premixed flames, illustrated by the bold black solid line in Fig. 12(a). The impact of multi dimensional wrinkled flame patterns induced by turbulent motions is difficult to quantify *a priori* as it depends of the subgrid flame wrinkling modeling [66]. However, if we neglect the influence of strain rate of the chemical flame structure, the maximum peak of CO is simply given by an instantaneous planar unstretched flame solution. The measured peak of CO is then located between an "steady laminar" upper limit given by steady laminar flame solution (which does not consider intermittency)

and "laminar intermittent" limit provided by the manufactured mean profile. It means that an LES simulation, which assumes the flamelet regime, will provide a solution between these two limits. An accurate computation of the resolved flame wrinkling combined with an efficient sub-grid scale flame wrinkling model may then hopefully provide the right answer.

The same procedure is now applied on a random distribution of thickened flame solutions. Results are plotted in Fig. 12(b) for a thickening factor of 4. While the upper limit is not affected by the artificial thickening, the lower limit is significantly increased, even exceeding the experimental data. An LES computation based on such thickened flame archetype would therefore never capture the chemical turbulent flame structure, no matter how accurate is the flame wrinkling resolution and modeling as the CO mass fraction would be systematically overestimated.

Fig. 13 shows, at three streamwise positions ($h = 6$, 15 and 30 mm), a comparison between the actual LES solution computed with TFLES model and the corresponding mean manufactured thickened flame solution. Three thickening factor are considered: F = 1.5, 4 and 8.5, corresponding to *Num I*, *Num D* and *Num A*, respectively. As expected, peak values of all LES solutions, obtained with a thickening factor F, lie between their corresponding lower boundary given by averaging laminar flamelets, also thickened with the same factor F, and the "steady laminar" boundary (given here by Y_{CO}=0.032). For large thickening factors (F = 4 and F = 8.5), "laminar intermittent" limit exceed the experimental data at the three axial location. Under these conditions, the LES will inevitably overpredict the CO production. The comparison also shows that for higher flame thickening factors, the TLES solutions are closer to the manufactured "intermittent laminar " flame brush limit. It means that the resolved 3-D flame wrinkling patterns are not significant anymore and the flame front is almost laminar. The reason is the lower sensitivity of the thickened flame to the resolved turbulent motion [68]. Logically, results obtained on the finest grid (Num I) present the best agreement against experimental data, since the flame is the least thickened.

Finally, it is worth noting that the non-premixed-based tabulation (green solid line in Fig. 10) yields better prediction than the premixed-based tabulation for Y_{CO} prediction in the outer flame region. This counter intuitive result is explained by two reasons. First, the non-premixed flame tabulation adopted by Group G [41,42] includes both
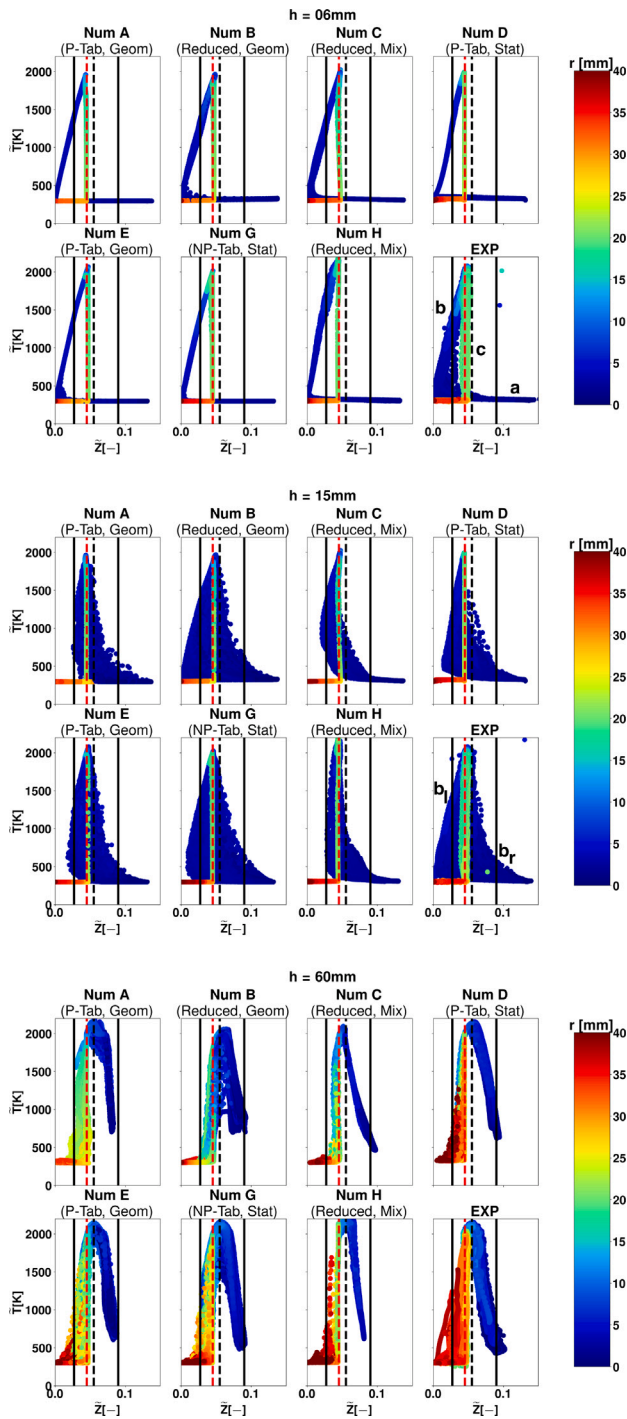
Fig. 16. Instantaneous scatter data for temperature versus mixture fraction Z at three axial locations. The vertical dashed line (black) in each plot marks the stoichiometric mixture fraction. The vertical solid lines (black) indicate the flammability limits and the vertical dashed line (red) correspond to slot 2 conditions. (For interpretation of the references to colour in this figure legend, the reader is referred to the web version of this article.)

of the steady and unsteady straining flamelets. The method captures the whole process of the flamelet straining and extinction, and results in a chemical database that is very similar to the premixed flame tabulation, especially when the straining rate is relatively low. Second this method does not employ artificial flame thickening, which biases the CO prediction as discussed previously.

4.5. Inner flame analysis: on the ability to capture multi-regime combustion

The analysis focuses now on the inner flame region (3 mm < r < 8 mm), where multi-regime combustion patterns are dominant [28]. Numerical solutions are again sorted by simplified chemistry assumption and turbulent combustion model approaches, in Figs. 14 and 15, respectively. As in the outer flame, the numerical solutions show a large dispersion around experimental data without any approach standing out from the others. Regarding the impact of simplified chemistry assumptions shown in Fig. 10, an expected source of modeling error is the inaccuracy of the premixed-flamelet manifold to capture multi-regime flame structure. However, this impact appears to be negligible compared to the bias induced by the artificial thickening of the flame, highlighted by the solid blue lines in Fig. 11, which is very similar to that observed in the analysis of the outer flame. Because of the multiple source of errors, it is difficult to draw a consolidated explanation of the simulations differences. However, we can note that despite the greater complexity of the inner flame structure, the results are not worse than the outer flame simulation.

4.6. Scatter plot analysis

The discussion now focuses on the ability of the approaches to qualitatively track chemical trajectories disregarding errors in flow prediction. For this purpose, scatter plots of temperature are first shown in Fig. 16 for the three axial positions h = 6, 15 and 60 mm. Data taken at the position h = 6 mm are located below the base of the lifted flame. Inert mixing between jet and air from slot 1 and between slot 1 and the outer flame products correspond to lines a and b shown in the experimental scatter plot. The vertical line c illustrates the premixed flame brush fed by slot 1 fresh gases. All simulations agree and capture these phenomena.

At h = 15 mm, reactions begin to occur in the inner flame region. The area covered by blue scatter plot illustrates reaction of samples located in the inner flame region. As discussed in [28], this region is characterized by the lines b_l and b_r, which correspond to the lean and rich boundaries, respectively. While all simulations capture the shape of the area covered by inner flame trajectories, significant differences are highlighted in the position of b_l and b_r. Moving farther downstream, the range of mixture fraction decrease, and numerical trajectories mainly agree with the experimental reference.

Scatter plots of CO mass fractions are shown in Fig. 17. While the production of CO is fairly captured above the burner exit (h = 6 mm) differences progressively increase when moving downstream. Significant differences are highlighted in both the amount of CO produced and the accessed trajectories, especially at h = 60 mm.

The Wasserstein metric [69,70] is now introduced to quantitatively compare the experimental and numerical scatter data. This postprocessing tool, defined as the weighted average of the pair-wise distances between samples of numerical (N) and experimental (E) distributions is well adapted to analyze combustion LES results [71,72]. Each element of the empirical distributions n_i and e_j contains information for three considered scalars: the mixture fraction Z, the temperature T and the CO mass fraction Y_{CO}. The 2nd Wasserstein metric is computed as solution of the following minimization problem:

$$W_2(Z, T, Y_{CO}) = \min_\Gamma \left(\sum_{i=1}^{n} \sum_{j=1}^{n'} \gamma_{ij} c_{ij} \right)^{1/2} \tag{1}$$

where Γ is the optimal transport matrix having elements γ_{ij} and dimension $n \times n'$. The unit transportation cost c_{ij} is defined as the 2nd power of the pair-wise Euclidean distance: $c_{ij} = \sum_{v=1}^{N_v} (n_{v,i} - e_{v,j})^2$, where v, is the vth of variable investigated, and N_v = 3 is the total number of scalar quantities. The Wasserstein metric is here applied to the MRB configuration at three axial locations corresponding to h = 6, 15 and 60 mm by using the code provided in [71]. Experimental and numerical
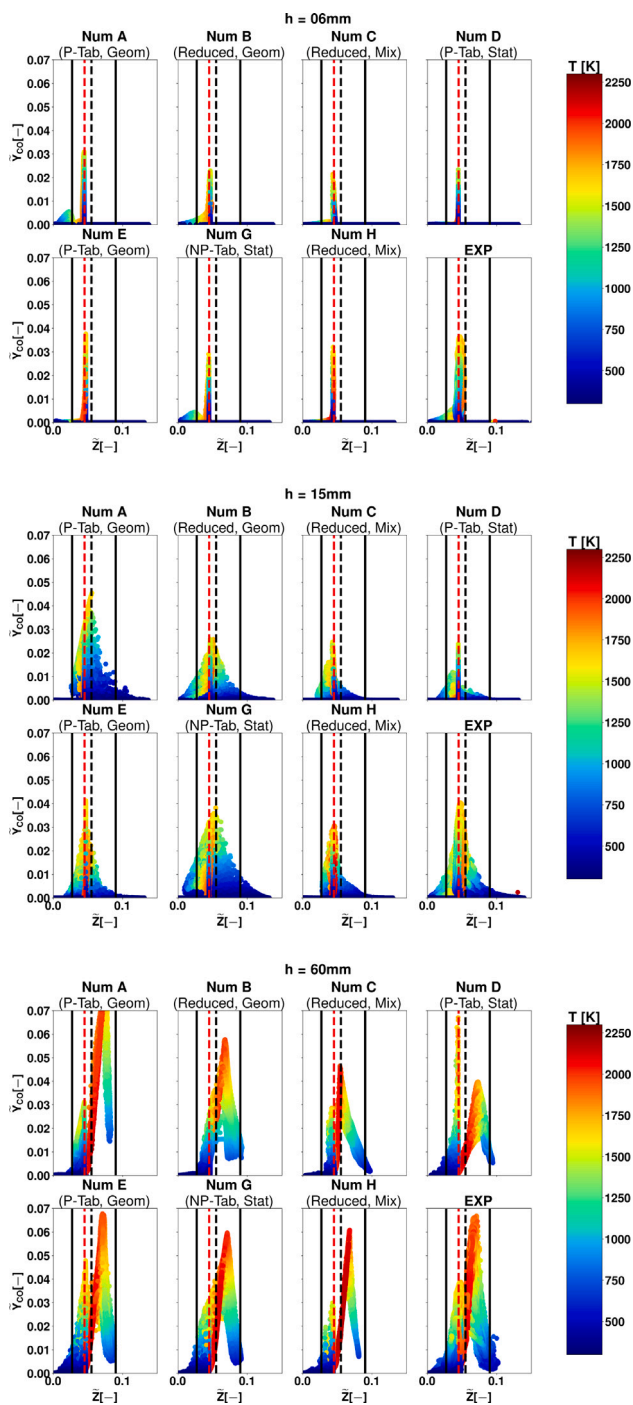
Fig. 17. Instantaneous scatter data for temperature versus mixture fraction Z at three axial locations. The vertical dashed line (black) in each plot marks the stoichiometric mixture fraction. The vertical solid lines (black) indicate the flammability limits and the vertical dashed line (red) correspond to slot 2 conditions. (For interpretation of the references to colour in this figure legend, the reader is referred to the web version of this article.)

scatter data are downsampled by selecting 1000 points. Figs. 18 and 19 shows the cumulative Wasserstein metric for all numerical solutions, normalized by the standard deviation of the experimental distribution. As in [71,72], the metric is decomposed in the single variable contributions to identify the source of error. The Wasserstein metrics are first sorted by type of chemistry model in Fig. 18. The cumulative and normalized metric $W_2(Z, T, Y_{CO})$ shows that tabulated chemistry performs as well as reduced chemistry, although it is *a priori* less accurate in multi-regime combustion. However the analysis by turbulent combustion model shown in Fig. 19 presents larger discrepancies in the geometrical approaches solutions, especially for temperature and CO.

This observation is consistent to the bias induced by the artificial flame front thickening previously discussed in 4.4.

4.7. Computational costs

Computational details are provided in Table 4. The reported data do not accurately compare code performance since different MPI implementations, compilers, interconnects, and CPU-cores were used. It highlights, however, the very large variation of the computational resources involved. The number of cores used by the groups varies by more than two orders of magnitude (from 108 to 65 536 cores). Also,
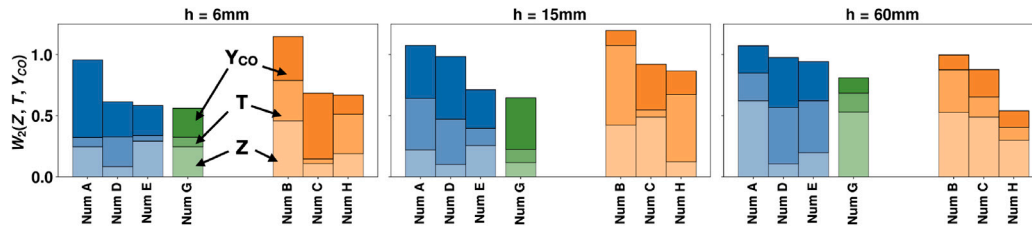
Fig. 18. Normalized cumulative multi-scalar 2nd Wasserstein metric for three different axial locations: h = 6, 15 and 60 mm. Simulations are sorted according to the chemistry modeling. Blue : premixed based tabulated chemistry. Green : non-premixed based tabulated chemistry. Orange: reduced chemistry. For each simulation results, the metric is decomposed in the three single variable contributions : mixture fraction, temperature and CO mass fraction (from bottom to top). (For interpretation of the references to colour in this figure legend, the reader is referred to the web version of this article.)
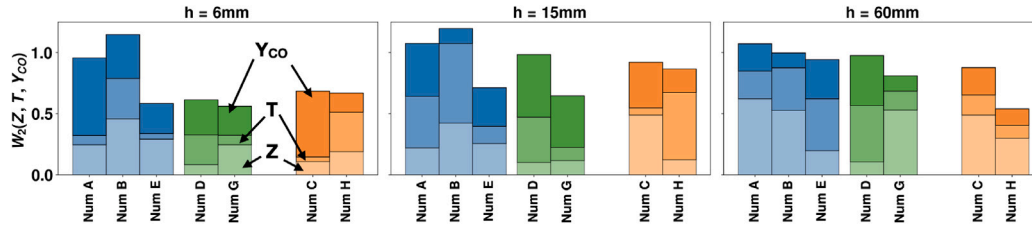

Fig. 19. Normalized cumulative multi-scalar 2nd Wasserstein metric for three different axial locations: h = 6, 15 and 60 mm. Simulations are sorted according to the turbulent combustion modeling. Blue : geometrical. Green : statistical. Orange: reactor-based. For each simulation results, the metric is decomposed in the three single variable contributions, from bottom to top: mixture fraction, temperature and CO mass fraction. (For interpretation of the references to colour in this figure legend, the reader is referred to the web version of this article.)

Table 4
Overview of the computations. The table shows the research groups with code name (C: Compressible; LM: Low Mach) , the type of processors with its clock rate, the number of cores, the core-hours, the simulated real time, the number of grid cells, the ratio of core time to real time and finally the computational cost (CC) defined as the ratio of core time to real time per cell.

Group code	Processors clock rate	N cores	T C-time	t sim-time	n cells	T/t	$T/t/n$ (CC)
–	–	1	10^3 h	s	10^6	1	1
A YALES2 LM	AMD Rome 2.6 GHz	768	354	0.12	31	10 624	**343**
B O.FOAM C	AMD EPYC 7442 2.25 GHz	128	116	0.48	4.34	876	**202**
C O.FOAM C	16-core Intel Haswell, 2.3 GHz	1 024	800	0.54	8	5 300	**666**
D O.FOAM C	AMD EPYC 7742 2.25 GHz	1 024	51	0.1	3.5	1 836	**524**
E O.FOAM LM	Xeon Platinum 817 3.1 GHz	1 200	244	0.08	31	11 000	**354**
F O.FOAM LM	AMD EPYC 7742 3.4 GHz	128	72	0.4	1	648	**648**
G O.FOAM LM	Xeon 2680 2.7 GHz	108	9.7	0.04	3.87	872	**226**
H O.FOAM C	Xeon E5–2603 1.6 GHz	240	73	0.11	3.5	2 389	**682**
I PsiPhi LM	AMD EPYC 7742 1.6 GHz	65 536	7 000	0.4	2 200	63 000	**28**

the differences between the cheapest and most expensive calculation are three orders of magnitude (from 9.7×10^3 to 7000×10^3 CPU hours). A measure of the computational cost (CC), independent of the grid size, is introduced as :

$$CC = \frac{T}{t \times n} \qquad (2)$$

where T, t, and n are the core time, the physical time, and the number of cells.

Being the only code to take advantage of structured connectivity, the PsiPhi code is much more efficient than OpenFoam and Yales 2 ($CC = 28$). The cost of simulations C and D is also affected by the use

of a compressible code that limits the time step to the acoustic scale. The differences between the other groups may be explained by the different categories of the turbulent combustion model. The efficiencies reached by simulations A, B, and E, which are based on a geometrical description of the turbulent flame propagation, are comparable ($CC = 202; 343; 353$). Simulations D and G, which used a presumed PDF formalism, presents a similar CPU cost ($CC = 226; 524$). Simulations obtained with the reactor-based approaches (groups C, F and H) are slightly more expensive as they require the local resolution of a detailed chemistry reactor model on each grid cell ($CC = 648; 666; 682$).

5. Conclusions

This joint numerical study of the MRB burner aims to partially illustrate the ability of the turbulent combustion modeling community in terms of multi-regime flame simulations. For that purpose, ten numerical groups and one experimental team collaborate within the framework of the TNF workshop. Simulations were performed on three different LES solvers: OpenFOAM (8 groups), YALES2 (1 group), and PsiPhi (1 group). Chemistry was simplified by using premixed flamelet tabulation (4 groups), non-premixed flamelet tabulation (1 group), and reduced chemical schemes (5 groups). The turbulent combustion models employed, representative of the three main modeling strategies, are the geometrical (4 groups), statistical (2 groups) and reactor based (3 groups) approaches. One team did account for subgrid scale fluctuation of chemical reaction rates. Different grid resolutions were employed with mesh sizes ranging between 1 million and 2.2 billion cells.

The comparison of 2-D instantaneous snapshots of heat release along the centerline planes evidenced a high sensitivity of the lift-off height prediction to the mesh resolution. Increasing the mesh resolution improves the prediction of mixing phenomena and therefore the location of the region where chemical reactions are initiated.

Detailed comparisons between experimental and numerical data along radial profiles taken at different axial positions showed that the temperature field is fairly captured by most of the computational strategies. However, the comparisons reveal significant discrepancies regarding CO mass fraction prediction. Three causes may explain this phenomenon:

1. A higher sensitivity of carbon monoxide to the simplification of detailed chemistry, especially when multiple combustion regimes are encountered.
2. A bias introduced by artificial thickening, which overestimates the species mass production rate.
3. The influence of the subgrid scale flame wrinkling on the filtered chemical flame structure, which is challenging to model for intermediate species [66].

Declaration of competing interest

The authors declare that they have no known competing financial interests or personal relationships that could have appeared to influence the work reported in this paper.

Data availability

Data will be made available on request.

Acknowledgments

Appendix A. Supplementary data

Supplementary material related to this article can be found online at https://doi.org/10.1016/j.jaecs.2023.100221.

References

[1] Masri A. Partial premixing and stratification in turbulent flames. Proc Comb Inst 2015;35:1115–36.

[2] Poinsot T, Veynante D. Theoritical and numerical combustion. RT Edwards, Inc.; 2005.

[3] Fiorina B, Cailler M. Accounting for complex chemistry in the simulations of future turbulent combustion systems. In: AIAA scitech 2019 forum. 2019.

[4] Turányi T. Reduction of large reaction mechanisms. New J Chem 1990;14:795–803.

[5] Pepiot-Desjardins P, Pitsch H. An efficient error-propagation-based reduction method for large chemical kinetic mechanisms. Combust Flame 2008;154:67–81.

[6] Goussis DA, Maas U. Model reduction for combustion chemistry. In: Turbulent combustion modeling. Springer; 2011, p. 193–220.

[7] Lu T, Law CK. Systematic approach to obtain analytic solutions of quasi steady state species in reduced mechanisms. J Phys Chem A 2006;110:13202–8.

[8] Maas U, Pope SB. Simplifying chemical kinetics: Intrinsic low-dimensional manifolds in composition space. Combust Flame 1992;88:239–64.

[9] Fiorina B, Veynante D, Candel S. Modeling combustion chemistry in large eddy simulation of turbulent flames. Flow Turbul Combust 2015;94:3–42.

[10] van Oijen J. Flamelet-generated manifolds: Development and application to premixed laminar flames (Ph.D. thesis), Technische Universiteit Eindhoven; 2002.

[11] Gicquel O, Darabiha N, Thévenin D. Laminar premixed hydrogen / air counterflow flame simulations using flame prolongation of ILDM with differential diffusion. Proc Comb Inst 2000;28:1901–8.

[12] Peters N. Laminar flamelet concepts in turbulent combustion. In: 21st symposium (int.) on combustion. The Combustion Institute; 1986, p. 1231–50.

[13] Pierce CD, Moin P. Progress-variable approach for large-eddy simulation of non-premixed turbulent combustion. J Fluid Mech 2004;504:73–97.

[14] Fiorina B, Gicquel O, Vervisch L, Carpentier S, Darabiha N. Approximating the chemical structure of partially premixed and diffusion counterflow flames using FPI flamelet tabulation. Combust Flame 2005;140:147–60.

[15] Westbrook CL, Dryer FL. Simplified reaction mechanisms for the oxidation of hydrocarbon fuels in flames. Combust Sci Technol 1981;27:31–43.

[16] Fernández-Tarrazo E, Sánchez AL, Liñán A, Williams FA. A simple one-step chemistry model for partially premixed hydrocarbon combustion. Combust Flame 2006;147:32–8.

[17] Cailler M, Darabiha N, Fiorina B. Development of a virtual optimized chemistry method, application to hydrocarbon/air combustion. Combust Flame 2020;211:281–302.

[18] Veynante D, Vervisch L. Turbulent combustion modeling. Prog Energy Combust 2002;28:193–266.

[19] Colin O, Ducros F, Veynante D, Poinsot T. A thickened flame model for large eddy simulations of turbulent premixed combustion. Phys Fluids 2000;12:1843–63.

[20] Fiorina B, Vicquelin R, Auzillon P, Darabiha N, Gicquel O, Veynante D. A filtered tabulated chemistry model for LES of premixed combustion. Combust Flame 2010;157:465–75.

[21] Charlette F, Meneveau C, Veynante D. A power-law flame wrinkling model for les of premixed turbulent combustion, part i: non-dynamic formulation. Combust Flame 2002;131:159–80.

[22] Wang G, Boileau M, Veynante D. Implementation of a dynamic thickened flame model for large eddy simulations of turbulent premixed combustion. Combust Flame 2011;158:2199–213.

[23] Haworth D. Progress in probability density function methods for turbulent reacting flows. Prog Energy Combust 2010;36:168–259.

[24] Péquin Arthur, Evans Michael J, Chinnici Alfonso, Medwell Paul R, Parente Alessandro. The reactor-based perspective on finite-rate chemistry in turbulent reacting flows: a review from traditional to low-emission combustion. Applications in Energy and Combustion Science 2023;16:100201. http://dx.doi.org/10.1016/j.jaecs.2023.100201.

[25] TNF Workshop, ????, International workshop on measurement and computation of turbulent flames.

[26] Kuenne G, Seffrin F, Fuest F, Stahler T, Ketelheun A, Geyer D, et al. Experimental and numerical analysis of a lean premixed stratified burner using 1D Raman/Rayleigh scattering and large eddy simulation. Combust Flame 2012;159:2669–89.

[27] Fiorina B, Mercier R, Kuenne G, Ketelheun A, Avdic A, Janicka J, et al. Challenging modeling strategies for LES of non-adiabatic turbulent stratified combustion. Combust Flame 2015;162:4264–82.

[28] Butz D, Hartl S, Popp S, Walther S, Barlow RS, Hasse C, et al. Local flame structure analysis in turbulent ch4/air flames with multi-regime characteristics. Combust Flame 2019;210:426–38.

[29] Popp S, Hartl S, Butz D, Geyer D, Dreizler A, Vervisch L, et al. Assessing multi-regime combustion in a novel burner configuration with large eddy simulations using tabulated chemistry. Proc Combust Inst 2021;38:2551–8.

[30] Massey JC, Li Z, Chen ZX, Tanaka Y, Swaminathan N. Large eddy simulation of multi-regime combustion with a two-progress variable approach for carbon monoxide. Proc Comb Inst 2023;39:2117–27.

[31] Butz D, Breicher A, Barlow R, Geyer D, Dreizler A. Turbulent multi-regime methane-air flames analysed by raman/rayleigh spectroscopy and conditional velocity field measurements. Combust Flame 2022;243:111941, A dedication to Professor Katharina Kohse-Höinghaus.

[32] Nicoud F, Toda HB, Cabrit O, Bose S, Lee J. Using singular values to build a subgrid-scale model for large eddy simulations. Phys Fluids 2011;23:085106.

[33] Yoshizawa A. Statistical theory for compressible turbulent shear flows, with the application to subgrid modeling. Phys Fluids 1986;29:2152–64.

[34] Ducros F, Nicoud F, Poinsot T. In: BMJ, editor. Wall-adapting local eddy-viscosity models for simulations in complex geometries. ICFD; 1998, p. 293–300.

[35] Germano M, Piomelli U, Moin P, Cabot WH. A dynamic subgrid-scale eddy viscosity model. Phys Fluids 1991;3:1760–5.

[36] Smagorinsky J. General circulation experiments with the primitive equations i, the basic experiment. Mon Weather Rev 1963;91:99–164.

[37] Hartl S, Geyer D, Dreizler A, Magnotti G, Barlow RS, Hasse C. Regime identification from raman/rayleigh line measurements in partially premixed flames. Combust Flame 2018;189:126–41.

[38] Moureau V, Domingo P, Vervisch L. Design of a massively parallel CFD code for complex geometries. CR Mech 2011;339:141–8.

[39] Kempf A, Geurts B, Oefelein J. Error analysis of large-eddy simulation of the turbulent non-premixed sydney bluff-body flame. Combust Flame 2011;158:2408–19.

[40] van Oijen JA, de Goey LPH. Modelling of premixed laminar flames using flamelet-generated manifolds. Combust Sci Technol 2000;161:113–37.

[41] Delhaye S, Somers L, van Oijen J, de Goey L. Incorporating unsteady flow-effects in flamelet-generated manifolds. Combust Flame 2008;155:133–44.

[42] Ma L, Huang X, Roekaerts D. Large eddy simulation of co2 diluted oxy-fuel spray flames. Fuel 2017;201:165–75, 1st International Workshop on Oxy-Fuel Combustion.

[43] Oijen JAV, Donini A, Bastiaans RJM, Boonkkamp JHMT, Goey LPHD. State-of-the-art in premixed combustion modeling using flamelet generated manifolds. Prog Energy Combust 2016;57:30–74.

[44] Péquin A, Iavarone S, Malpica Galassi R, Parente A. The partially stirred reactor model for combustion closure in large eddy simulations: Physical principles, sub-models for the cell reacting fraction, and open challenges. Phys Fluids 2022;34:055122.

[45] Golovitchev V, Chomiak J. Numerical modeling of high temperature air flame-less combustion. In: Proceedings of the 4th international symposium on high temperature air combustion and gasification. 2001, p. 761–74.

[46] Ertesvåg IS, Magnussen BF. The eddy dissipation turbulence energy cascade model. Combust Sci Technol 2000;159:213–35.

[47] Toshimitsu K, Matsuo A, Kamel MR, Morris CI, Hanson RK. Numerical simulations and planar laser-induced fluorescence imaging results of hypersonic reactive flows. J Propuls Power 2000;16:16–21.

[48] Gargiulo G, Ciottoli P, Martelli E, Galassi RM, Valorani M. Numerical analysis of laser-pulse transient ignition of oxygen/methane mixtures in rocket-like combustion chamber. Acta Astronaut 2019;159:136–55.

[49] Ruan S, Swaminathan N, Darbyshire O. Modelling of turbulent lifted jet flames using flamelets: a priori assessment and a posteriori validation. Combust Theory Model 2014;18:295–329.

[50] Chen Z, Ruan S, Swaminathan N. Large eddy simulation of flame edge evolution in a spark-ignited methane–air jet. Proc Comb Inst 2017;36:1645–52.

[51] Massey JC, Chen ZX, Swaminathan N. Modelling heat loss effects in the large eddy simulation of a lean swirl-stabilised flame. Flow Turbul Combust 2021;106:1355–78.

[52] Zhang K, Dybe S, Shen YZ, Schimek S, Paschereit CO, Duwig C. Experimental and numerical investigation of ultra-wet methane combustion technique for power generation. In: Turbo expo: Power for land, sea, and air. ASME; 2021, GT2020–16105.

[53] Lu T, Law CK. Toward accommodating realistic fuel chemistry in large-scale computations. Prog Energy Combust 2009;35:192–215.

[54] Floyd J, Kempf AM, Kronenburg 1 A, Ram R. A simple model for the filtered density function for passive scalar combustion LES. Combust Theory Model 2009;13:559–88.

[55] Donini A, Bastiaans R, van Oijen J, de Goey L. A 5-D implementation of fgm for the large eddy simulation of a stratified swirled flame with heat loss in a gas turbine combustor. Flow Turbul Combust 2017;98:887–922.

[56] Lu T, Law CK. A criterion based on computational singular perturbation for the identification of quasi steady state species: A reduced mechanism for methane oxidation with no chemistry. Combust Flame 2008;154:761–74.

[57] Popp S. Large eddy simulation of turbulent multi-regime combustion: potentials and limitations of flamelet-based chemistry modeling (Ph.D. thesis), Technische Universität Darmstadt; 2020.

[58] Nambully S, Domingo P, Moureau V, Vervisch L. A filtered-laminar-flame PDF sub-grid scale closure for LES of premixed turbulent flames. part I: Formalism and application to a bluff-body burner with differential diffusion. Combust Flame 2014;161:1756–74.

[59] Nambully S, Domingo P, Moureau V, Vervisch L. A filtered-laminar-flame PDF sub-grid-scale closure for LES of premixed turbulent flames, part II: Application to a stratified bluff-body burner. Combust Flame 2014;161:1775–91.

[60] Zhang W, Karaca S, Wang J, Huang Z, van Oijen J. Large eddy simulation of the cambridge/sandia stratified flame with flamelet-generated manifolds: Effects of non-unity lewis numbers and stretch. Combust Flame 2021;227:106–19.

[61] Engelmann L, Wollny P, Breicher A, Geyer D, Chakraborty N, Kempf A. Numerical analysis of multi-regime combustion using flamelet generated manifolds - a highly-resolved large-eddy simulation of the darmstadt multi-regime burner. Combust Flame 2023;251:112718. http://dx.doi.org/10.1016/j.combustflame.2023.112718, URL https://www.sciencedirect.com/science/article/pii/S0010218023001037.

[62] Gruhlke P, Inanc E, Mercier R, Fiorina B, Kempf AM. A simple post-processing method to correct species predictions in artificially thickened turbulent flames. Proc Combust Inst 2021;38:2977–84.

[63] Maio G, Cailler M, Mercier R, Fiorina B. Virtual chemistry for temperature and CO prediction in LES of non-adiabatic turbulent flames. Proc Combust Inst 2019;37:2591–9.

[64] Benard P, Lartigue G, Moureau V, Mercier R. Large-eddy simulation of the lean-premixed preccinsta burner with wall heat loss. Proc Comb Inst 2019;37:5233–43.

[65] Vervisch L, Domingo P, Lodato G, Veynante D. Scalar energy fluctuations in large-eddy simulation of turbulent flames: Statistical budgets and mesh quality criterion. Combust Flame 2010;157:778–89.

[66] Mercier R, Mehl C, Fiorina B, Moureau V. Filtered wrinkled flamelets model for large-eddy simulation of turbulent premixed combustion. Combust Flame 2019;205:93–108.

[67] Moureau V, Domingo P, Vervisch L. From large-eddy simulation to direct numerical simulation of a lean premixed swirl flame: Filtered laminar flame-PDF modeling. Combust Flame 2011;158:1340–57.

[68] Auzillon P, Fiorina B, Vicquelin R, Darabiha N, Gicquel O, Veynante D. Modeling chemical flame structure and combustion dynamics in LES. Proc Combust Inst 2011;33:1331–8.

[69] Dudley RM. Probabilities and metrics: Convergence of laws on metric spaces, with a view to statistical testing, volume 45. Aarhus Universitet, Matematisk Institut; 1976.

[70] Pele O, Werman M. Fast and robust earth mover's distances. In: 2009 IEEE 12th international conference on computer vision. IEEE; 2009, p. 460–7.

[71] Johnson R, Wu H, Ihme M. A general probabilistic approach for the quantitative assessment of les combustion models. Combust Flame 2017;183:88–101.

[72] Maio G, Cailler M, Darabiha N, Fiorina B. Capturing multi-regime combustion in turbulent flames with a virtual chemistry approach. Proc Combust Inst 2021;38:2559–69. http://dx.doi.org/10.1016/j.proci.2020.06.131, URL https://www.sciencedirect.com/science/article/pii/S1540748920302054.